

Hybrid Analytical Modeling: Fourier Modeling Combined With Mesh-Based Magnetic Equivalent Circuits

K. J. W. Pluk, J. W. Jansen, and E. A. Lomonova

Department of Electrical Engineering, Eindhoven University of Technology, Eindhoven 5612 AZ, The Netherlands

This paper presents a hybrid analytical modeling (HAM) method, which integrates a mesh-based magnetic equivalent circuit model with the Fourier modeling approach. This HAM is capable of correctly predicting the electromagnetic field distributions for various 2-D geometries. The generalized approach of the presented hybrid modeling concept makes the modeling technique applicable to a wide range of electromagnetic devices. By only meshing the parts of the domain in the vicinity of the high-permeable materials, the increase in computational effort is limited compared with the sole use of Fourier modeling. The proposed HAM method predicts the force in the geometry with $\geq 97\%$ accuracy with respect to finite-element analysis.

Index Terms—Analytical models, electromagnetic modeling, Fourier analysis, magnetic equivalent circuit (MEC), reluctance network.

NOMENCLATURE

\vec{A}	Magnetic vector potential [Wb m ⁻¹].
\vec{B}	Magnetic flux density vector [T].
\vec{H}	Magnetic field strength vector [A m ⁻¹].
\vec{J}	Current density [A m ⁻²].
\vec{M}_0	Magnetization vector [A m ⁻¹].
\hat{e}	Unit vector [—].
B_r	Remanent flux density [T].
μ_0	Permeability of vacuum $4\pi \cdot 10^{-7}$ [H m ⁻¹].
μ_r	Relative permeability [—].
i	Arbitrary Fourier region [—].
m	Arbitrary MEC-region [—].
k	Arbitrary MEC-element number [—].
ψ	Magnetic scalar potential [A].
ϕ	Magnetic flux [Wb].
ω_n^i	Spatial frequency [m ⁻¹].
n	Harmonic number [—].
N	Total number of harmonics [—].
x_p	Width of the periodicity [m].

I. INTRODUCTION

ELECTROMAGNETIC field modeling is a crucial step in the design process of electromagnetic devices. A very extensive magnetic field modeling is necessary to achieve an optimal design. A lot of research and development is conducted in methods to predict the magnetic field distribution inside electromagnetic structures. In particular, during the design of an electromagnetic device, the computational efforts should be low to enable a broad exploratory investigation of the design space. Therefore, the numerical methods (such as finite-element analysis (FEA) [1]) are less convenient, and if possible the reduction from a 3-D geometry to a 2-D model is made.

Manuscript received November 18, 2014; revised February 4, 2015; accepted March 23, 2015. Date of publication April 2, 2015; date of current version July 20, 2015. Corresponding author: K. J. W. Pluk (e-mail: k.j.w.pluk@tue.nl).

Color versions of one or more of the figures in this paper are available online at <http://ieeexplore.ieee.org>.

Digital Object Identifier 10.1109/TMAG.2015.2419197

Analytical or semianalytical modeling methods are less time consuming than the numerical methods, however, usually the accuracy that can be obtained with these methods is lower. During the design, the accuracy of the magnetic field calculations is less important, which makes the semianalytical modeling methods a suitable way to predict the magnetic field. In the literature, many semianalytical methods are discussed, including the following:

- 1) magnetic equivalent circuit (MEC) modeling [2], [3];
- 2) (surface) charge modeling (CM) [4]–[7];
- 3) Fourier modeling [8]–[11].

For applications, where the flux paths are largely predefined by the high-permeable materials, the MEC modeling is usually the appropriate choice. This predefined path enables the usage of flux tubes to simplify the geometry, and therewith, enables the calculation of the magnetic field. To apply the MEC modeling to more complex geometries, the modeling can be extended with the tooth contour method [12] or a conformal mapping technique [13]. The extension enables the calculation of the nonarbitrary couplings between, for instance, the stator and the rotor.

For unbounded problems, where no coils and no high-permeable material are present, the surface CM is one of the preferable options. The surface CM is extended by applying images [14], [15] or by including the secondary magnetic field [16] to mimic the high-permeable materials in the vicinity.

Geometries with repeating geometrical patterns are a typical example for a spatial harmonic description, such as Fourier modeling. Using the Fourier modeling, the different materials are incorporated as regions, where in each region, a Fourier-based expression for the magnetic field is used. However, this definition is limited to regions, and therefore materials, of equal width (in the periodic direction). Extending the Fourier modeling with mode matching, regions (i.e., material blocks) with a different width can be incorporated [9], [17]. Unfortunately, an additional physically nonexisting boundary is necessary to obtain a solution. Furthermore, in situations where small features are important, the number of harmonics can be limited due to

TABLE I
GEOMETRICAL AND MATERIAL PARAMETERS
FOR SHIELDING GEOMETRY

Parameter	Value	Description
x_p	100 [mm]	Width of the periodicity
x_{mz}	20 [mm]	Width of magnets in z -direction
x_{mx}	5 [mm]	Width of magnets in x -direction
x_g	14 [mm]	Width of the hole in the shield
x_t	4 [mm]	Width of the thickening of the shield
x_{vcm}	10 [mm]	Width of the voice coil magnet
x_{vcb}	10 [mm]	Width of the voice coil bundle
$x_{c,vcb}$	29 [mm]	Center of the voice coil bundle
$x_{c,vcm}$	43 [mm]	Center of the voice coil magnet
z_m	20 [mm]	Height of the magnets
z_g	10 [mm]	Gap between magnets and shield
z_{s1}	1 [mm]	Thickness of the shield
z_{s2}	2 [mm]	Thickness of the shield with thickening
z_{vc}	20 [mm]	Height of the voice coil
$z_{b,vc}$	35 [mm]	Bottom coordinate of the voice coil
B_r	1.4 [T]	Remanence of the permanent magnets
J	5 [A/mm ²]	Current density in voice coil
$\mu_{r,m}$	1.05 [—]	Relative permeability of magnets
$\mu_{r,s}$	1500 [—]	Relative permeability of the shield

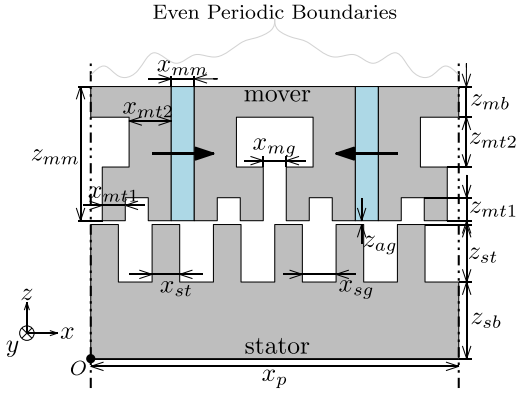


Fig. 2. Multitooth flux-switching permanent magnet linear motor geometry.

TABLE II
GEOMETRICAL AND MATERIAL PARAMETERS FOR
MULTITOOTH MOTOR GEOMETRY

Parameter	Value	Description
x_p	48 [mm]	Width of the periodicity
x_{st}	3.6 [mm]	Width stator teeth
x_{sg}	4.4 [mm]	Width of gap between stator teeth
x_{mt1}	3 [mm]	Width of small mover teeth
x_{mg}	3 [mm]	Width of gap between small mover teeth
x_{mm}	3 [mm]	Width of mover magnets
x_{mt2}	5.5 [mm]	Width of large mover teeth
z_{sb}	10 [mm]	Height of stator backiron
z_{st}	7.5 [mm]	Height of stator teeth
z_{ag}	0.5 [mm]	Height of airgap
z_{mt1}	3 [mm]	Height of small mover teeth
z_{mt2}	6.5 [mm]	Height of large mover teeth
z_{mb}	4 [mm]	Height of mover backiron
z_{mm}	17.5 [mm]	Height of mover magnet
B_r	1.2 [T]	Remanence of the permanent magnets
$\mu_{r,m}$	1 [—]	Relative permeability of magnets
$\mu_{r,i}$	750 [—]	Relative permeability of the iron

C. Division in Regions

Observing the geometries shown in Figs. 1 and 2, the coordinate system is defined such that the present periodicity is aligned with the x -axis and the invariant direction is chosen in the y -direction. The z -direction is the direction with

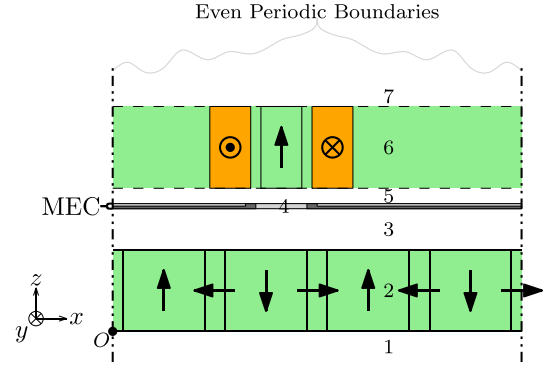


Fig. 3. Division in regions for the shielding geometry shown in Fig. 1.

the changing materials. For the HAM, the geometry should be divided in regions where each region contains only one material and has a width equal to the periodicity. The regions are numbered ascending in the z -direction.

A permanent magnet is incorporated in the modeling as a region containing the magnetic material, while the permanent magnet is represented by a block-shaped magnetization function. Equivalently, the coil bundles are modeled by a region with $\mu_r = 1$ [—] and a block-shaped current density function (see Region 6 in Fig. 3).

In general, in the HAM, all high-permeable materials ($\mu_r \gg 10$) that do not have a width equal to the periodicity are modeled using an MEC region. Inside this MEC region, all materials (high permeable, but also air) and sources are meshed. Therefore, in the geometry of Fig. 1, the magnetic shield with its thickened parts is modeled using the mesh-based MEC modeling.

For the geometry in Fig. 2, the Stator teeth are modeled as an MEC region, while the full mover is modeled as another MEC region. The obtained MEC regions have a width equal to the periodicity, while the mesh inside the MEC regions is chosen such that the material changes are incorporated.

The resulting division in regions for the shielding geometry is given in Fig. 3, where Region 4 is the MEC region. For the multitooth motor, Regions 3 and 5 are MEC regions, as shown in Fig. 4, where the division in regions is shown. Throughout this paper, a general definition of the regions is used, where i is an arbitrary Fourier region, while m is used for the MEC region.

D. Definition of MEC Element

As previously indicated, inside the MEC region, a mesh-based discretization is used. The MEC region is meshed in the x -direction with rectangular elements. Even though the meshing in both the x -direction and the z -direction can be nonuniform, in the used formulation, all elements in the z -direction with a certain x -coordinate will have an equal width in the x -direction and vice versa. The meshing of the MEC region is performed such that the material boundaries of the geometry are coinciding with the edges of the MEC elements. The number of MEC elements inside the MEC region can be increased for a more accurate solution.

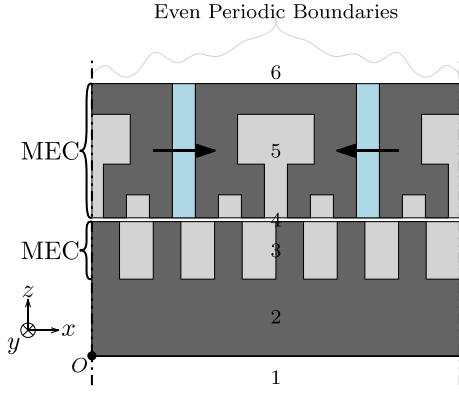


Fig. 4. Division in regions for the multitooth flux-switching permanent magnet linear motor of Fig. 2.

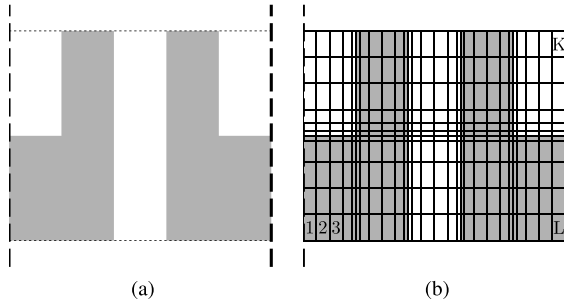


Fig. 5. Meshing principle illustrated on a simplified system where (a) geometry and (b) obtained meshing, including numbering and locally increased mesh density [dashed (vertical) lines: periodic boundaries].

Due to the possibility of a nonuniform mesh size, local increase of mesh density is possible. However, in the used formulation, a local increase of the mesh in the x -direction will be visible throughout the full z -direction of the MEC region as shown in Fig. 5 (where the numbering of the mesh elements is indicated as well).

With the described meshing method, the resulting MEC elements will contain only one material (i.e., iron, air or magnet). In each MEC element, a potential node is defined in its geometrical center. From this potential node toward all four sides of the MEC element, a magnetic reluctance is present. In both the positive and the negative x -direction, a reluctance is assumed, which covers half of the width of the MEC element. While the reluctances in the positive and negative z -direction each cover half of the height of the MEC element. The reluctances used are calculated according to

$$\mathcal{R}_{x+}^k = \mathcal{R}_{x-}^k = \frac{l_x^k}{2\mu_0\mu_r^k S_{yz}^k} \quad (1)$$

$$\mathcal{R}_{z+}^k = \mathcal{R}_{z-}^k = \frac{l_z^k}{2\mu_0\mu_r^k S_{xy}^k} \quad (2)$$

where l_x^k and l_z^k are the sizes of MEC-element k in the x -direction and z -direction, respectively, where $\mu_0 = 4\pi \cdot 10^{-7}$ [H/m] is the permeability of vacuum, μ_r^k is the relative permeability of the material in this MEC element. Furthermore, S_{xy}^k and S_{yz}^k are the cross-sectional areas of

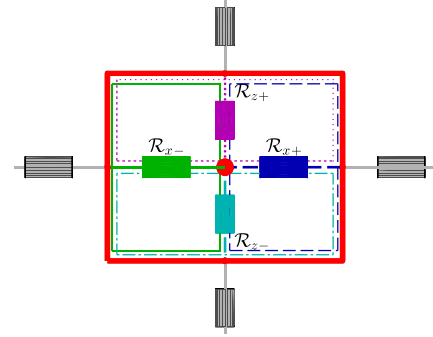


Fig. 6. Mesh element in the mesh-based MEC modeling. Thick red solid-line square: actual MEC element. Red circular marker: potential node. Reluctance elements: \mathcal{R}_{x+} , \mathcal{R}_{x-} , \mathcal{R}_{z+} , and \mathcal{R}_{z-} .

MEC-element k in the xy -plane and yz -plane, respectively. Due to the assumption of a 2-D geometry, a unity size of an MEC element in the y -direction is chosen.

The reluctances in each MEC element are shown in Fig. 6, where the thick (red) solid-line rectangle indicates the actual mesh element, and the red point gives the potential node. Furthermore, the solid, dashed, dotted, and dashed-dotted lines illustrate the flux tubes corresponding with the reluctance elements.

With the reluctances, the center node is coupled to the adjacent MEC elements on the top, bottom, left, and right to complete the MEC region. The periodicity inside the MEC region is considered by assuming that the last element in the x -direction is adjacent to the first element in the x -direction and vice versa.

III. MODELING METHODOLOGY

A. Fourier Modeling Description

To solve the magnetostatic field distribution in a region, the magnetic flux density, \vec{B} , can be written in terms of the magnetic vector potential, \vec{A} , as explained in [9]. By assuming a 2-D geometry with the invariance in the y -direction, where the magnetization is only possible in the x -direction and z -direction and is independent of z , and where only a current density in the y -direction exists, a second-order differential equation is obtained as

$$\nabla^2 A_y(x, z) = -\mu_0\mu_r J_y(x) + \mu_0 \frac{\partial M_z(x)}{\partial x} \quad (3)$$

where μ_r is the relative permeability of the material in the region, J_y is the current density in the y -direction, and M_z is the residual magnetization in the z -direction.

In each region, the solution for A_y^i , where i is an arbitrary region with a Fourier description, is chosen such that the Poisson equation (3) is fulfilled while concerning the periodicity in the x -direction. The chosen general solution for A_y is given by

$$A_y^i(x, z) = A_{y0}^i(z) + \sum_{n=1}^N [A_{ycn}^i(z) \cos(\omega_n^i x) + A_{ysn}^i(z) \sin(\omega_n^i x)] \quad (4)$$

where N is the total number of harmonics considered, and $A_{y0}^i(z)$, $A_{ycn}^i(z)$, and $A_{ysn}^i(z)$ are given by

$$A_{y0}^i(z) = -\mu_0 M_{x0}^i z \quad (5)$$

$$A_{ycn}^i(z) = -\frac{1}{\omega_n^i} q_n^i e^{\omega_n^i z} - \frac{1}{\omega_n^i} r_n^i e^{-\omega_n^i z} - \frac{\mu_0}{\omega_n^i} M_{zsn}^i - \frac{\mu_0 \mu_r}{(\omega_n^i)^2} J_{ycn}^i \quad (6)$$

$$A_{ysn}^i(z) = -\frac{1}{\omega_n^i} s_n^i e^{\omega_n^i z} - \frac{1}{\omega_n^i} t_n^i e^{-\omega_n^i z} + \frac{\mu_0}{\omega_n^i} M_{zcn}^i - \frac{\mu_0 \mu_r}{(\omega_n^i)^2} J_{ysn}^i \quad (7)$$

where q_n^i , r_n^i , s_n^i , and t_n^i are the *a priori* unknown coefficients, which have to be solved using boundary conditions, and where M_{zsn}^i , M_{zcn}^i , J_{ysn}^i , and J_{ycn}^i are the sine and cosine terms of the Fourier description of the magnetization in the z -direction and the current density in the y -direction, respectively. Furthermore, M_{x0}^i is the dc term in the magnetization in the x -direction, which will occur in the boundary description of the tangential magnetic field strength (later on), and ω_n^i is n times the fundamental spatial frequency ω_0 , which is determined from the periodicity according to

$$\omega_n^i = n\omega_0 = n\frac{2\pi}{x_p} \quad (8)$$

where x_p is the width of the periodicity.

With the given definition of the magnetic vector potential, the magnetic flux density description can be derived according to

$$\vec{B}^i(x, z) = -\frac{\partial A_y^i(x, z)}{\partial z} \hat{e}_x + \frac{\partial A_x^i(x, z)}{\partial x} \hat{e}_z. \quad (9)$$

The magnetic flux density inside an arbitrary Fourier region is given by

$$\vec{B}^i(x, z) = B_x^i(x, z) \hat{e}_x + B_z^i(x, z) \hat{e}_z \quad (10)$$

$$B_x^i(x, z) = \mu_0 M_{x0}^i + \sum_{n=1}^N [B_{xsn}^i(z) \sin(\omega_n^i x) + B_{xcn}^i(z) \cos(\omega_n^i x)] \quad (11)$$

$$B_z^i(x, z) = \sum_{n=1}^N [B_{zsn}^i(z) \sin(\omega_n^i x) + B_{zcn}^i(z) \cos(\omega_n^i x)] \quad (12)$$

where B_{xsn}^i , B_{xcn}^i , B_{zsn}^i , and B_{zcn}^i are given by

$$B_{xsn}^i(z) = s_n^i e^{\omega_n^i z} - t_n^i e^{-\omega_n^i z} \quad (13)$$

$$B_{xcn}^i(z) = q_n^i e^{\omega_n^i z} - r_n^i e^{-\omega_n^i z} \quad (14)$$

$$B_{zsn}^i(z) = q_n^i e^{\omega_n^i z} + r_n^i e^{-\omega_n^i z} + \mu_0 M_{zsn}^i + \frac{\mu_0 \mu_r}{\omega_n^i} J_{ycn}^i \quad (15)$$

$$B_{zcn}^i(z) = -s_n^i e^{\omega_n^i z} - t_n^i e^{-\omega_n^i z} + \mu_0 M_{zcn}^i - \frac{\mu_0 \mu_r}{\omega_n^i} J_{ysn}^i. \quad (16)$$

B. Source Term Description

In the magnetic flux density description, the magnetization and current density terms are derived as a Fourier description. In general, a permanent magnet will be replaced by a rectangular-shaped magnetization function. Equivalently, a rectangular-shaped current density function is assumed. These magnetization and current density functions are described as

$$M_x^i(x) = M_{x0}^i + \sum_{n=1}^N [M_{xsn}^i \sin(\omega_n^i x) + M_{xcn}^i \cos(\omega_n^i x)] \quad (17)$$

$$M_z^i(x) = M_{z0}^i + \sum_{n=1}^N [M_{zsn}^i \sin(\omega_n^i x) + M_{zcn}^i \cos(\omega_n^i x)] \quad (18)$$

$$J_y^i(x) = J_{y0}^i + \sum_{n=1}^N [J_{ysn}^i \sin(\omega_n^i x) + J_{ycn}^i \cos(\omega_n^i x)]. \quad (19)$$

Except for M_{x0} , all dc terms can be neglected, since only M_{x0} is required in the Fourier description. The sine and cosine terms of the magnetization in the x -direction are not directly visible in the magnetic flux density description, however, these terms are used in the boundary conditions.

According to the general Fourier theory [9], the source terms (i.e., M_{x0} , M_{xsn} , M_{xcn} , M_{z0} , M_{zsn} , M_{zcn} , J_{y0} , J_{ysn} , and J_{ycn}), when considering the rectangular-shaped definition of the source curves, are given by

$$M_{x0}^i = \frac{1}{x_p} \sum_{s_x^i=1}^{S_x^i} \hat{M}_{x^i}^{s_x^i} (x_1^{s_x^i} - x_0^{s_x^i}) \quad (20)$$

$$M_{xsn}^i = \frac{2}{x_p} \sum_{s_x^i=1}^{S_x^i} \frac{\hat{M}_{x^i}^{s_x^i}}{\omega_n^i} (\cos(\omega_n^i x_0^{s_x^i}) - \cos(\omega_n^i x_1^{s_x^i})) \quad (21)$$

$$M_{xcn}^i = \frac{2}{x_p} \sum_{s_x^i=1}^{S_x^i} \frac{\hat{M}_{x^i}^{s_x^i}}{\omega_n^i} (\sin(\omega_n^i x_1^{s_x^i}) - \sin(\omega_n^i x_0^{s_x^i})) \quad (22)$$

where s_x^i is a counter through the magnets magnetized in the x -direction in region i , and x_0 and x_1 are the x -coordinate of the left and right sides of the magnet, respectively, and where $\hat{M}_{x^i}^{s_x^i}$ is the amplitude of the magnetization of this magnet. Equivalently, the source terms for M_z and J_y are found.

A permanent magnet for which the magnetization is not aligned with either the x -direction or the z -direction is modeled by superimposing a magnet magnetized in the x -direction, and a magnet magnetized in the z -direction. The strength of these magnets is obtained using the vector projection on the axis of the original magnetization.

C. MEC Modeling Description

The harmonic modeling method described above is limited to describing situations where the high-permeable material spans the full period of the model. The inclusion of small high-permeable features (such as tooth tips, slot shapes, and small slots) is not directly possible. Therefore, the mesh-based MEC modeling technique is applied to model the

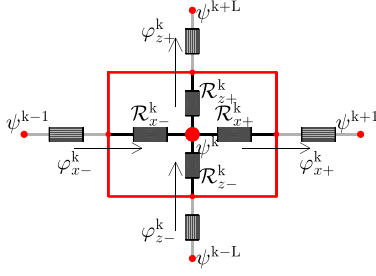


Fig. 7. Magnetic flux, ϕ , reluctance, \mathcal{R} , and magnetic potential, ψ , involved in the magnetic equivalent of Kirchhoff's current law (23).

high-permeable features that are smaller than the period of the Fourier model.

As previously indicated, inside each MEC element a potential-node is defined. With the magnetic equivalence of Kirchhoff's current law, the magnetic scalar potential distribution in the center nodes of the MEC elements in the MEC region is found. The magnetic equivalence of Kirchhoff's current law applied to MEC-element k (shown in Fig. 7) gives

$$\sum \phi_{in} = \sum \phi_{out} \Rightarrow \phi_{x-} + \phi_{z-} - \phi_{x+} - \phi_{z+} = 0 \quad (23)$$

where ϕ is the magnetic flux in a branch, calculated according to

$$\phi_{x-}^k = \frac{\psi^{k-1} - \psi^k}{\mathcal{R}_{x+}^{k-1} + \mathcal{R}_{x-}^k} \quad (24)$$

$$\phi_{x+}^k = \frac{\psi^k - \psi^{k+1}}{\mathcal{R}_{x-}^{k+1} + \mathcal{R}_{x+}^k} \quad (25)$$

$$\phi_{z-}^k = \frac{\psi^{k-L} - \psi^k}{\mathcal{R}_{z+}^{k-L} + \mathcal{R}_{z-}^k} \quad (26)$$

$$\phi_{z+}^k = \frac{\psi^k - \psi^{k+L}}{\mathcal{R}_{z-}^{k+L} + \mathcal{R}_{z+}^k} \quad (27)$$

where ψ^k is the magnetic scalar potential at the center node of MEC-element k , and L is the number of MEC elements in a layer of the MEC region (i.e., all elements in the MEC region with an equal z -coordinate). Therefore, MEC-element $k+L$ is directly on the top of element k .

To include the periodicity in the MEC layer, for the far left and far right MEC elements, their adjacent MEC elements in the x -direction are replaced according to

$$k-1 = k-1+L \quad \text{for } k=1+qL \quad (28)$$

$$k+1 = k+1-L \quad \text{for } k=L+qL \quad (29)$$

where $q = 0, 1, \dots, K/L - 1$, and K is the total number of MEC elements in the region. The top and bottom layer of the MEC region are linked to the Fourier regions that are adjacent at the top or bottom. From the MEC region, the Fourier regions are considered to be a flux source, therefore, these sources are coupled, as shown in Fig. 8.

The amplitude of the flux sources is calculated by

$$\phi_{z-}^k = \iint B_z^{m-1}(x, z) \Big|_{z=h_b} dS_{xy} \quad (30)$$

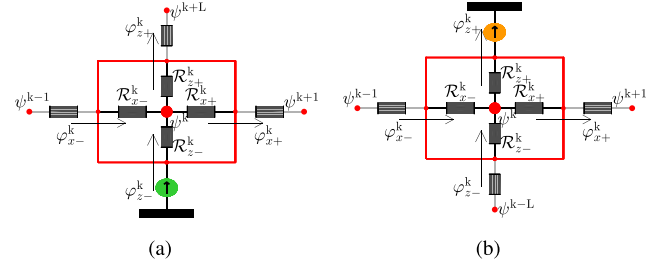


Fig. 8. Coupling between the MEC region and the Fourier region at (a) bottom and (b) top.

which is the total amount of flux entering through the cross-sectional area at the bottom of an MEC element in the bottom layer of the MEC region (region m), where h_b is the z -coordinate of the boundary between the involved regions (i.e., the MEC region and the Fourier region underneath). Evaluating the integrations for a unit depth in the y -direction, the strength of the flux source is given by

$$\phi_{z-}^k = \sum_{n=1}^N \left[\frac{-1}{\omega_n^{m-1}} (\cos(\omega_n^{m-1} x_1^k) - \cos(\omega_n^{m-1} x_0^k)) B_{zsn}^{m-1}(h_b) + \frac{1}{\omega_n^{m-1}} (\sin(\omega_n^{m-1} x_1^k) - \sin(\omega_n^{m-1} x_0^k)) B_{zcn}^{m-1}(h_b) \right] \quad (31)$$

where B_{zsn} and B_{zcn} are given by (15) and (16), respectively, and x_0^k and x_1^k are the left and right x -coordinate of MEC-element k , respectively, and k is bounded by $1 \leq k \leq L$, which are all MEC elements in the bottom layer. Equivalently, the flux at the top of an MEC element in the top layer of the MEC region is calculated, with the Fourier description in region $m+1$ and for MEC-elements $K-L+1 \leq k \leq K$.

IV. BOUNDARY CONDITIONS

Inside each Fourier and MEC region, the description of the magnetic field is now defined. To apply the Maxwell's equations throughout the whole domain, these equations should hold on the boundaries between the regions as well. Applying Maxwell's equations to the boundary results in the continuity of both the magnetic flux density normal to the boundary and the magnetic field strength, \vec{H} , tangential with the boundary, at the z -coordinate of this boundary ($z = h_b$). Therefore, the boundary conditions are given by

$$B_z^i(x, z) \Big|_{z=h_b} = B_z^{i+1}(x, z) \Big|_{z=h_b} \quad (32)$$

$$H_x^i(x, z) \Big|_{z=h_b} = H_x^{i+1}(x, z) \Big|_{z=h_b}. \quad (33)$$

Using the constitutive relation, $\vec{B} = \mu_0 \mu_r \vec{H} + \mu_0 \vec{M}_0$, with \vec{M}_0 the residual magnetization, (33) becomes

$$\frac{\mu_r^{i+1}}{\mu_r^i} B_x^i(x, h_b) - \frac{\mu_0 \mu_r^{i+1}}{\mu_r^i} M_x^i(x) = B_x^{i+1}(x, h_b) - \mu_0 M_x^{i+1}(x). \quad (34)$$

A. Boundary Conditions Between Fourier Regions

When both regions i and $i+1$ are Fourier regions, the continuity of the normal magnetic flux density and the tangential magnetic field strength is included by means of

the separation of variables. Since both regions i and $i + 1$ have an equal width of the periodicity, their fundamental frequencies are equal. This implies that a separation of the sine and cosine functions is valid, and therefore, for every harmonic n , (32) is given by

$$B_{zsn}^i(h_b) = B_{zsn}^{i+1}(h_b) \quad (35)$$

$$B_{zcn}^i(h_b) = B_{zcn}^{i+1}(h_b). \quad (36)$$

The tangential magnetic field boundary condition (34) for every harmonic n is given by

$$\frac{\mu_r^{i+1}}{\mu_r^i} B_{xsn}^i(h_b) - \frac{\mu_0 \mu_r^{i+1}}{\mu_r^i} M_{xsn}^i = B_{xsn}^{i+1}(h_b) - \mu_0 M_{xsn}^{i+1} \quad (37)$$

$$\frac{\mu_r^{i+1}}{\mu_r^i} B_{xcn}^i(h_b) - \frac{\mu_0 \mu_r^{i+1}}{\mu_r^i} M_{xcn}^i = B_{xcn}^{i+1}(h_b) - \mu_0 M_{xcn}^{i+1}. \quad (38)$$

With these equations, $4N$ boundary equations are obtained to solve, together with the other boundary conditions, the $4N$ unknowns inside a Fourier region (i.e., q_n , r_n , s_n , and t_n).

B. Boundary Conditions Between Fourier and MEC Region

The continuity of the normal magnetic flux density and the tangential magnetic field strength should hold on the boundary between a Fourier region and an MEC region as well. Since the magnetic flux density in the z -direction is used as a flux source in the MEC elements connected to the bottom and top layer of the MEC region, the continuity of the normal magnetic flux density is already covered.

To ensure the continuity of the tangential magnetic field strength, (34) is rewritten for the MEC region, given by

$$\frac{\mu_r^k}{\mu_r^{m-1}} B_x^{m-1}(x, h_b) - \frac{\mu_0 \mu_r^k}{\mu_r^{m-1}} M_x^{m-1}(x) = B_x^k(x, h_b) - \mu_0 M_x^k(x) \quad (39)$$

where k is the MEC element for the observed x -coordinate, and $m - 1$ is the Fourier region underneath the MEC region. The magnetic flux density in the x -direction for MEC-element k is found by dividing the average flux in the x -direction by its cross-sectional area

$$B_x^k(x, h_b) = \frac{1}{2S_{yz}^k} (\phi_{x-}^k + \phi_{x+}^k) \quad (40)$$

where ϕ_{x-} and ϕ_{x+} are given in (24) and (25), respectively. Substituting the general expression (11) for the magnetic flux density in the x -direction for a Fourier region, the tangential magnetic field boundary condition, which should hold for all MEC elements at the boundary, is given by

$$\begin{aligned} & \sum_{n=1}^N [(B_{xsn}^{m-1}(h_b) - \mu_0 M_{xsn}^{m-1}) \sin(\omega_n^{m-1} x) \\ & + (B_{xcn}^{m-1}(h_b) - \mu_0 M_{xcn}^{m-1}) \cos(\omega_n^{m-1} x)] \\ & = \frac{\mu_r^{m-1}}{2\mu_r^k S_{yz}^k} \left(\frac{\psi^{k-1} - \psi^k}{\mathcal{R}_{x+}^{k-1} + \mathcal{R}_{x-}^k} + \frac{\psi^k - \psi^{k+1}}{\mathcal{R}_{x+}^k + \mathcal{R}_{x-}^{k+1}} \right) - \frac{\mu_0 \mu_r^{m-1}}{\mu_r^k} M_x^k \end{aligned} \quad (41)$$

where $B_{xsn}^{m-1}(h_b)$ and $B_{xcn}^{m-1}(h_b)$ are given by (13) and (14) with assuming that $z = h_b$, the z -coordinate of the boundary between the MEC region and the Fourier region.

Inside the MEC region, the distribution of the tangential magnetic flux density is a staircase-shaped function, due to the constant magnetic flux density assumed inside the MEC elements. This staircase-shaped function is described as a Fourier series. Due to the separation of the sine and cosine terms, the tangential magnetic field equations are given by

$$\begin{aligned} & s_n^{m-1} e^{\omega_n^{m-1} h_b} - t_n^{m-1} e^{-\omega_n^{m-1} h_b} - \mu_0 M_{xsn}^{m-1} \\ & + \frac{2\mu_r^{m-1}}{x_p \omega_n^{m-1}} \sum_{k=1}^L \left[\left\{ \frac{1}{2\mu_r^k S_{yz}^k} \left(\frac{\psi^{k-1} - \psi^k}{\mathcal{R}_{x+}^{k-1} + \mathcal{R}_{x-}^k} + \frac{\psi^k - \psi^{k+1}}{\mathcal{R}_{x+}^k + \mathcal{R}_{x-}^{k+1}} \right) \right. \right. \\ & \left. \left. + \frac{-\mu_0}{\mu_r^k} M_x^k \right\} (\cos(\omega_n^{m-1} x_1^k) - \cos(\omega_n^{m-1} x_0^k)) \right] \\ & = 0 \end{aligned} \quad (42)$$

$$\begin{aligned} & q_n^{m-1} e^{\omega_n^{m-1} h_b} - r_n^{m-1} e^{-\omega_n^{m-1} h_b} - \mu_0 M_{xcn}^{m-1} \\ & + \frac{-2\mu_r^{m-1}}{x_p \omega_n^{m-1}} \sum_{k=1}^L \left[\left\{ \frac{1}{2\mu_r^k S_{yz}^k} \left(\frac{\psi^{k-1} - \psi^k}{\mathcal{R}_{x+}^{k-1} + \mathcal{R}_{x-}^k} + \frac{\psi^k - \psi^{k+1}}{\mathcal{R}_{x+}^k + \mathcal{R}_{x-}^{k+1}} \right) \right. \right. \\ & \left. \left. + \frac{-\mu_0}{\mu_r^k} M_x^k \right\} (\sin(\omega_n^{m-1} x_1^k) - \sin(\omega_n^{m-1} x_0^k)) \right] \\ & = 0 \end{aligned} \quad (43)$$

where the summation over all L elements in the bottom layer of the MEC region is performed. By taking the average magnetic flux in MEC-element k , the magnetic scalar potential of three different MEC elements (i.e., MEC-element k and its adjacent elements in the x -direction) is used in each term of the summation. Since the summation is cyclic over the bottom layer [see (28) and (29)], the equations can be rewritten toward

$$\begin{aligned} & s_n^{m-1} e^{\omega_n^{m-1} h_b} - t_n^{m-1} e^{-\omega_n^{m-1} h_b} + \frac{\mu_r^{m-1}}{2S_{yz}} \frac{2}{x_p \omega_n^{m-1}} \sum_{k=1}^L \\ & \times \left[\frac{1}{\mu_r^{k-1}} \frac{-1}{\mathcal{R}_{x+}^{k-1} + \mathcal{R}_{x-}^k} \cos(\omega_n^{m-1} x) \Big|_{x=x_0^{k-1}}^{x=x_1^{k-1}} \right. \\ & + \frac{1}{\mu_r^k} \left(\frac{-1}{\mathcal{R}_{x+}^{k-1} + \mathcal{R}_{x-}^k} + \frac{1}{\mathcal{R}_{x+}^k + \mathcal{R}_{x-}^{k+1}} \right) \cos(\omega_n^{m-1} x) \Big|_{x=x_0^k}^{x=x_1^k} \\ & + \frac{1}{\mu_r^{k+1}} \frac{1}{\mathcal{R}_{x+}^k + \mathcal{R}_{x-}^{k+1}} \cos(\omega_n^{m-1} x) \Big|_{x=x_0^{k+1}}^{x=x_1^{k+1}} \Big] \psi^k = \mu_0 M_{xsn}^{m-1} \\ & + \sum_{k=1}^L \left[\frac{2\mu_r^{m-1}}{x_p \omega_n^{m-1} \mu_r^k} M_x^k (\cos(\omega_n^{m-1} x_1^k) - \cos(\omega_n^{m-1} x_0^k)) \right] \end{aligned} \quad (44)$$

$$\begin{aligned} & q_n^{m-1} e^{\omega_n^{m-1} h_b} - r_n^{m-1} e^{-\omega_n^{m-1} h_b} + \frac{-\mu_r^{m-1}}{2S_{yz}} \frac{2}{x_p \omega_n^{m-1}} \sum_{k=1}^L \\ & \times \left[\frac{1}{\mu_r^{k-1}} \frac{-1}{\mathcal{R}_{x+}^{k-1} + \mathcal{R}_{x-}^k} \sin(\omega_n^{m-1} x_1^{k-1}) \Big|_{x=x_0^{k-1}}^{x=x_1^{k-1}} \right. \\ & + \frac{1}{\mu_r^k} \left(\frac{-1}{\mathcal{R}_{x+}^{k-1} + \mathcal{R}_{x-}^k} + \frac{1}{\mathcal{R}_{x+}^k + \mathcal{R}_{x-}^{k+1}} \right) \sin(\omega_n^{m-1} x_1^k) \Big|_{x=x_0^k}^{x=x_1^k} \\ & + \frac{1}{\mu_r^{k+1}} \frac{1}{\mathcal{R}_{x+}^k + \mathcal{R}_{x-}^{k+1}} \sin(\omega_n^{m-1} x_1^{k+1}) \Big|_{x=x_0^{k+1}}^{x=x_1^{k+1}} \Big] \psi^k = \mu_0 M_{xcn}^{m-1} \\ & + \sum_{k=1}^L \left[\frac{-2\mu_r^{m-1}}{x_p \omega_n^{m-1} \mu_r^k} M_x^k (\sin(\omega_n^{m-1} x_1^k) - \sin(\omega_n^{m-1} x_0^k)) \right]. \end{aligned} \quad (45)$$

For the continuity of the tangential magnetic field at the top of the MEC region, (44) and (45) are used for MEC-elements $K - L + 1 \leq k \leq K$ and for the Fourier quantities of region $m + 1$.

C. Noncontinuous Boundary Conditions

In addition to the continuous boundaries, other boundary conditions are applicable as well. For a region, which has one of its boundaries at $z = \pm\infty$, the magnetic field will vanish toward the boundary. For a Fourier region, this boundary condition is given by

$$B_x^i(x, z)|_{z=\pm\infty} = 0 \quad (46)$$

$$B_z^i(x, z)|_{z=\pm\infty} = 0. \quad (47)$$

Since no sources can exist, which have an infinite size, the results from boundary condition derived from B_x and B_z become equal. The boundary conditions are, therefore, given by

$$B_{xsn}^i(z)|_{z=\pm\infty} = 0 \quad (48)$$

$$B_{xcn}^i(z)|_{z=\pm\infty} = 0. \quad (49)$$

Substituting (13) and (14), this is simplified to

$$r_n^I = 0 \quad \& \quad t_n^I = 0 \quad \text{if } z = -\infty \quad (50)$$

$$q_n^I = 0 \quad \& \quad s_n^I = 0 \quad \text{if } z = \infty \quad (51)$$

where I shows the last region of the geometry.

Inside an MEC region, the same kind of boundary condition can hold if it is assumed that no magnetic field can escape the MEC region at one of the sides (i.e., the magnetic field is tangential with the boundary). For these situations, the flux in the z -direction on one of the boundary interfaces is assumed to be zero, therefore, this boundary condition is implemented by assuming that the flux toward this boundary is zero or, equivalently, the reluctance (in the z -direction) toward this boundary is infinite, given by

$$\text{If } m = 1, \quad \mathcal{R}_{z-}^k = \infty \quad \text{for } 1 \leq k \leq L \quad (52)$$

$$\text{If } m = I, \quad \mathcal{R}_{z+}^k = \infty \quad \text{for } K - L + 1 \leq k \leq K. \quad (53)$$

Finally, the condition that the magnetic field is fully perpendicular to the boundary is concerned. This boundary condition is equivalent with assuming that the material located on the other side of the boundary has an infinite permeability. This means that the magnetic flux density parallel to the boundary interface, B_x , is zero, therefore, the following boundary equation is used:

$$B_x^i(x, z)|_{z=h_b} = \mu_0 M_x(x) \quad (54)$$

where h_b is the z -coordinate of the boundary plane. For a Fourier region, (54) can directly be implemented by

$$B_{xsn}^i(h_b) = \mu_0 M_{xsn} \quad (55)$$

$$B_{xcn}^i(h_b) = \mu_0 M_{xcn}. \quad (56)$$

For an MEC region, the boundary condition of (54) is mimicked by assuming that the reluctances in the x -direction

TABLE III
EQUATIONS USED FOR BOUNDARY CONDITIONS OF FOURIER REGION

Type	Continuous		MEC	Zero-flux	$\mu = \infty$
	Top	Bottom			
Sine	(35)	(37)	(44)	(48)	(55)
Cosine	(36)	(38)	(45)	(49)	(56)

inside the layer of MEC elements that are the closest to the boundary interface are infinite, as given by

$$\mathcal{R}_{x-}^k = \infty \quad \text{and} \quad \mathcal{R}_{x+}^k = \infty \quad (57)$$

where the boundary elements k are denoted by

$$1 \leq k \leq L \quad \text{if } m = 1 \quad (58)$$

$$K - L + 1 \leq k \leq K \quad \text{if } m = I. \quad (59)$$

Due to implying an infinite x -reluctance throughout the full layer of MEC elements that are the closest to the boundary, no magnetic flux in the x -direction is assumed in this layer of MEC elements. Therefore, to increase the accuracy of the solution, the size in the z -direction of the elements adjacent to the boundary should be taken small.

V. CALCULATING THE COEFFICIENTS

All boundary conditions are known, therefore, the unknown coefficients are solvable. For each Fourier region, $4N$ *a priori* unknown coefficients are used (i.e., q_n , r_n , s_n , and t_n). Furthermore, both at the top and bottom of each Fourier region, N equations concerning the sine terms and N equations concerning the cosine terms are obtained, independent of the type of boundary conditions used, as shown in Table III. While for the MEC region, there are K unknown coefficients (i.e., ψ^k), for which K independent equations are given [based on Kirchhoff's current law (23)].

To solve all unknowns, the boundary conditions and coefficients are collected in one matrix equation, given by

$$\underbrace{\begin{bmatrix} E_b^1 \\ E_t^1 \\ E_b^2 \\ \vdots \\ E_b^{m-1} \\ E_{MEC}^{m-1} \\ E_{KCL} \\ E_{MEC}^{m+1} \\ E_t^{m+1} \\ E_b^{m+2} \\ \vdots \\ E_t^I \end{bmatrix}}_{E_{tot}} \underbrace{\begin{bmatrix} Q^1 \\ Q^2 \\ \vdots \\ Q^{m-1} \\ \Psi \\ Q^{m+1} \\ Q^{m+2} \\ \vdots \\ Q^I \end{bmatrix}}_X = \underbrace{\begin{bmatrix} Y_b^1 \\ Y_t^1 \\ Y_b^2 \\ \vdots \\ Y_b^{m-1} \\ Y_{MEC}^{m-1} \\ Y_{KCL} \\ Y_{MEC}^{m+1} \\ Y_t^{m+1} \\ Y_b^{m+2} \\ \vdots \\ Y_t^I \end{bmatrix}}_{Y_{tot}} \quad (60)$$

where E are the sine and cosine equations of the boundary conditions of the Fourier region (according to Table III) with trailing and/or leading zeros to ensure the connection to the correct coefficients, Y are the terms in the boundary conditions that are not dependent on the unknown coefficients

(i.e., the source terms), $\mathbf{Q} = [\mathbf{q}_n, \mathbf{r}_n, \mathbf{s}_n, \mathbf{r}_n]^T$ represents the column vector with Fourier unknowns, and Ψ is a column vector with the magnetic potential inside all MEC elements. Furthermore, the subscripts b and t represent the bottom and top of the region, while E_{MEC} is given by (44) and (45), and E_{kel} is given by (23), and where I indicates the last region considered.

Before solving this set of matrix equations, the coefficients that are directly found by a boundary condition [i.e., (50) and (51)] should be removed from the set of equations, together with the corresponding boundary conditions. Afterward, the matrix equation (60) is solved using a lower-upper-decomposition, and all the (*a priori*) unknown coefficients are found.

VI. FORCE CALCULATION

With all coefficients defined, the magnetic flux density throughout the whole domain is known, therefore, for calculation of the force on a part of the geometry, the Maxwell stress tensor is applied. By defining the integration domain as a closed box around the part of the domain for which the force desired (including air), an accurate calculation of the force is obtained with a numerical integration. As derived in [26], the force density per unit depth on a 2-D geometry is given by

$$F_x = \frac{1}{\mu_r \mu_0} \left\{ - \int_{C_b} B_x B_z dx - \int_{C_l} \left(\frac{1}{2} B_x^2 - \frac{1}{2} B_z^2 \right) dz + \int_{C_t} B_x B_z dx + \int_{C_r} \left(\frac{1}{2} B_x^2 - \frac{1}{2} B_z^2 \right) dz \right\} \quad (61)$$

$$F_z = \frac{1}{\mu_r \mu_0} \left\{ - \int_{C_b} \left(\frac{1}{2} B_z^2 - \frac{1}{2} B_x^2 \right) dx - \int_{C_l} B_z B_x dz + \int_{C_t} \left(\frac{1}{2} B_z^2 - \frac{1}{2} B_x^2 \right) dx + \int_{C_r} B_z B_x dz \right\} \quad (62)$$

where C_b , C_l , C_t , and C_r are the bottom, left, top, and right edges of the integration domain, respectively.

VII. MODEL VALIDATION

The proposed HAM method is validated using 2-D FEA models for the shielding and multitooth motor geometry given in Figs. 1 and 2, respectively. The 2-D FEA models are implemented in FLUX2D [27] and are densely meshed, while the periodicity, and all material properties and geometrical parameters are equal to the implemented hybrid analytical models.

For the shielding geometry, shown in Fig. 1, the magnitude of the magnetic flux density obtained with the HAM is shown in Fig. 9(a). As it is visible, a smooth magnetic flux density pattern is obtained with the proposed hybrid method. In Fig. 9(b), the difference between the FEA results and the HAM results is shown as $\Delta|B| = |B_{\text{FEA}}| - |B_{\text{HAM}}|$. In the regions, where the permanent magnets are located, the

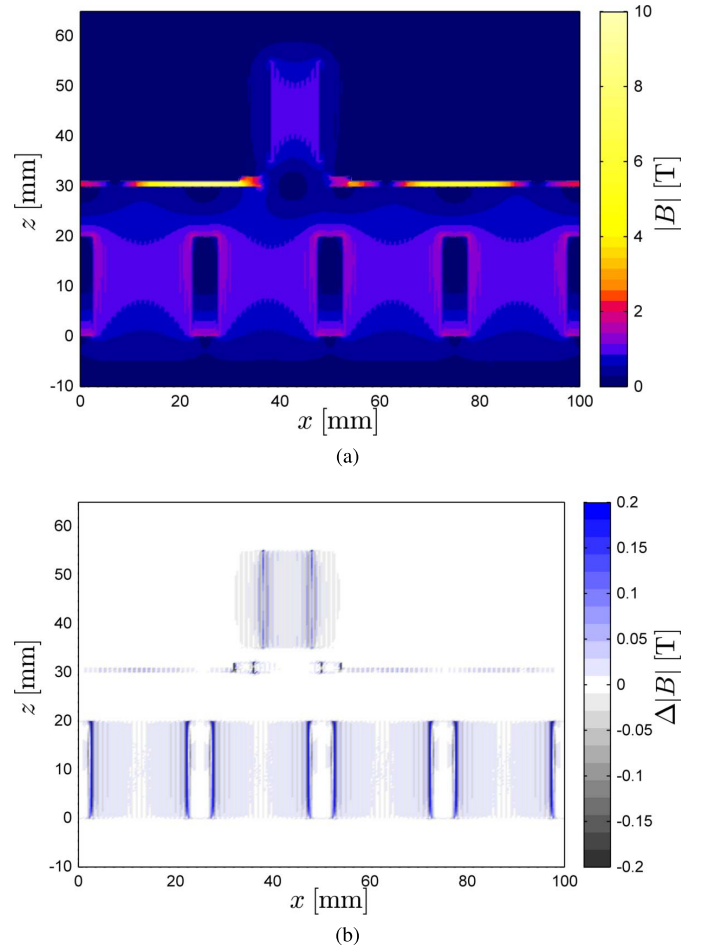


Fig. 9. Magnetic flux density for the shielding geometry of Fig. 1 with (a) absolute value obtained with the proposed HAM and (b) difference between FEA and HAM, $\Delta|B| = |B_{\text{FEA}}| - |B_{\text{HAM}}|$. $N = 100$ harmonics are used in all Fourier regions and an $x \times z$ -discretization of 265×22 is used in Region 4.

harmonic description of the permanent magnets is clearly visible (i.e., the Gibbs phenomenon [28]). For the permanent magnet of the voice coil, a deviation is visible that is extending further in the x -direction than inside the magnet array. Furthermore, some deviations are shown inside the MEC region. These deviations are mainly due to the discretization of the MEC-region, where the magnetic flux density contains discrete steps instead of the desired smooth pattern.

A more thorough comparison between the results obtained, with FEA and the hybrid analytical model, for the shielding geometry is given in Fig. 10, where the magnetic flux density on a path in the middle of the shield ($z = 30.5$ [mm]) is shown.

Observing B_x and B_z , the HAM closely matches the FEA results. However, the differences, shown in Fig. 10(c), clearly reveal the deviations. For the magnetic flux density in the x -direction, a discretization noise is visible, the amplitude of the noise increases with the derivative of B_x . Furthermore, for both B_x and B_z , there are deviations visible around the edges of the shield (at $x = 36$ [mm] and $x = 50$ [mm]). The remaining large differences are located around the edges of the thickening of the shield.

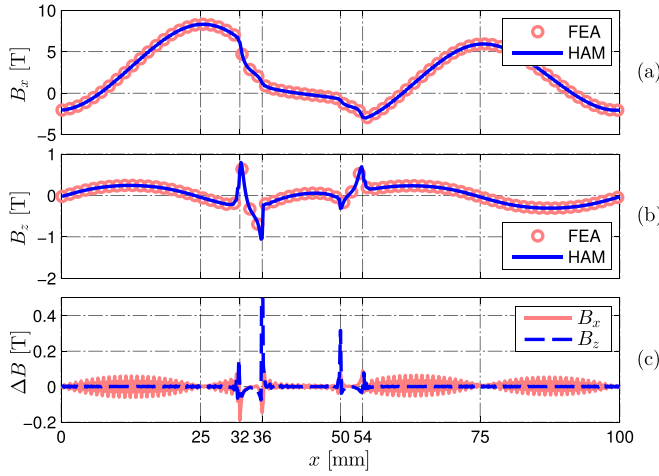


Fig. 10. Magnetic flux density in the middle of the shield ($z = 30.5$ [mm]) for the FEA and HAM. (a) Magnetic flux density in the x -direction. (b) Magnetic flux density in the z -direction. (c) Difference between FEA and HAM, $\Delta|B| = |B_{FEA}| - |B_{HAM}|$.

TABLE IV
FORCE ON PERMANENT MAGNET OF VOICE-COIL ACTUATOR AND
MOVER OF MULTITOOTH MOTOR

	Voice-coil		Multi-tooth motor	
	F_x [N/m]	F_z [N/m]	F_x [N/m]	F_z [N/m]
FEA	121.6	327.5	238	$-15.9 \cdot 10^{-3}$
HAM	121.6	317.7	235	$-16.0 \cdot 10^{-3}$
ΔF [N/m]	-0.05	9.83	3.02	141
ΔF [%]	-0.05	3.09	2.24	-0.89

For a numerical comparison, the force per unit depth in the x -direction and z -direction on the permanent magnet of the voice-coil actuator obtained from FEA and HAM is given in Table IV. In addition to the calculated force, the difference in force between the FEA and the HAM is given, where $\Delta F_x \ll 1$ [%] and $\Delta F_z \approx 3$ [%].

For the multitooth motor geometry, shown in Fig. 2, the absolute value of the magnetic flux density obtained with HAM is shown in Fig. 11(a). Again, a rather smooth magnetic flux density pattern is obtained with the proposed hybrid method. In Fig. 11(b), the difference between the FEA results and the HAM results is shown as $\Delta|B| = |B_{FEA}| - |B_{HAM}|$. In addition to the edges of the high-permeable material, only small deviations are visible.

A more thorough comparison between the finite element and hybrid analytical results for the multitooth motor is given in Fig. 12, where the magnetic flux density in the center of the air gap ($z = 17.75$ [mm]) is shown.

The HAM is visually similar with the FEA results when observing the B_x and B_z . The difference between the FEA and the HAM, shown in Fig. 12(c), clearly shows a deviation between the models. Most of these deviations, for both B_x and B_z , occur around the edges of the teeth of either the stator or the mover. Note that it is well known that an accurate prediction of the magnetic flux density obtained with FEA is not ensured around the edges of a material.

For a numerical comparison, the force per unit depth on the mover in the x -direction and z -direction calculated from FEA and HAM is given in Table IV. In addition to

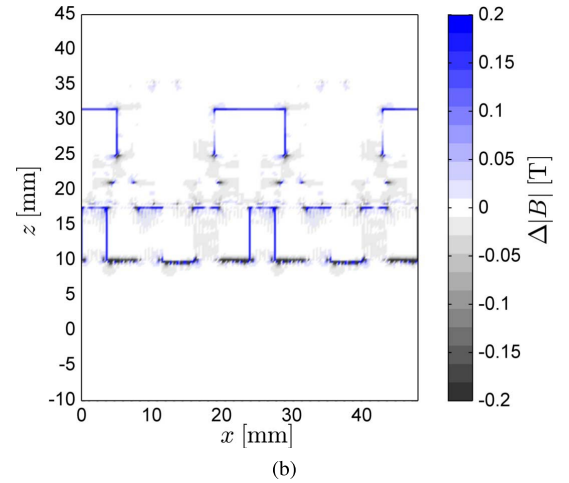
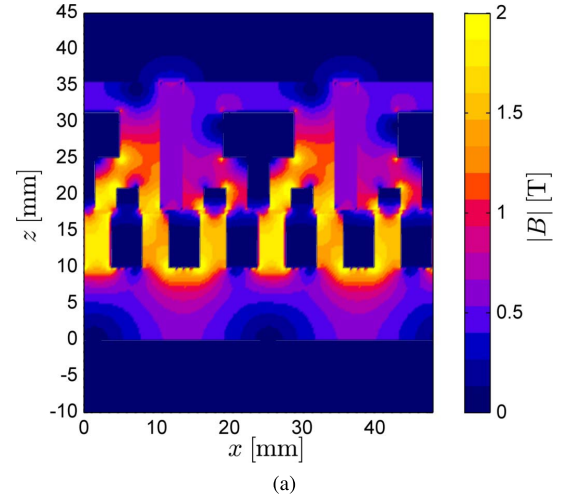


Fig. 11. Magnetic flux density for the multitooth motor geometry of Fig. 2 with (a) absolute value obtained with the proposed HAM and (b) difference between FEA and HAM, $\Delta|B| = |B_{FEA}| - |B_{HAM}|$. $N = 100$ harmonics are used in all Fourier regions, and an $x \times z$ -discretization of 127×33 and 225×73 is used in Regions 3 and 5, respectively.

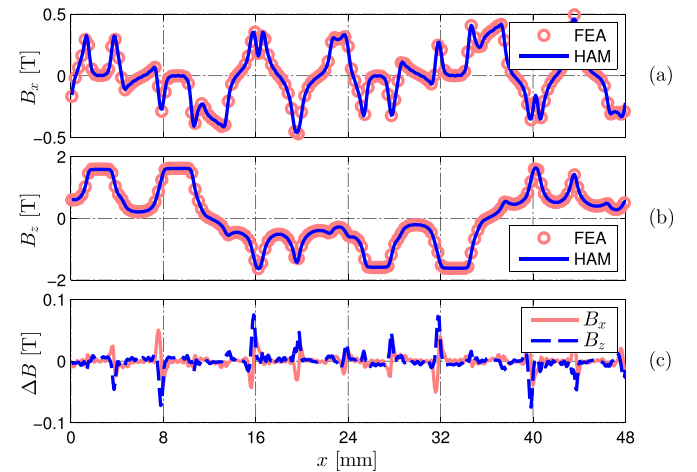


Fig. 12. Magnetic flux density in the middle of the air gap ($z = 17.75$ [mm]) of Fig. 2 for FEA and HAM. (a) Magnetic flux density in the x -direction. (b) Magnetic flux density in the z -direction. (c) Difference between (FEA) and HAM, $\Delta|B| = |B_{FEA}| - |B_{HAM}|$.

the calculated force, the difference in force between the FEA and the HAM is given, where $\Delta F_x < 1.5$ [%] and $\Delta F_z < 1$ [%].

TABLE V
SIMULATION PARAMETERS FOR VOICE-COIL ACTUATOR AND
MULTITOOTH MOTOR FOR HAM. N IS NUMBER OF HARMONICS AND
TIME IS SIMULATION TIME, INCLUDING MESHING,
SOLVING, AND CALCULATING B -FIELD AND FORCE

	Voice-coil HAM	Multi-tooth motor HAM
N	100	100
mesh-size	265×22	97×33 169×73
Time [min]	1.25	12

The simulation parameters for the HAM are given in Table V. For the MEC regions, the number of mesh elements is: “number of mesh elements in x ” \times “number of mesh elements in z ”. The simulation time includes meshing, solving and calculation of the B -field and force.

VIII. DISCUSSION

In Section VII, it has been shown that the magnetic flux density distribution found with the proposed hybrid 2-D model with respect to 2-D FEA gives accurate results. In the proposed HAM method, the benefits of two analytical modeling methods are combined, i.e., Fourier modeling and mesh-based MEC modeling. Both analytical modeling methods have some drawbacks, which have been highlighted in Section VII.

The differences in the predicted magnetic flux density inside the regions with a permanent magnet clearly reveals the harmonic description (i.e., Gibbs phenomenon). The deviations occurring are due to the description of a rectangular-shaped magnetization function with a number of harmonics. A more noticeable difference is visible in Region 6 when compared with Region 2 in Fig. 9(b). The deviations between the models extends further in the x -direction in Region 6 due to the assumption of a full region with one single permeability. In the HAM, the full region has the permeability of the permanent magnet, while the FEA only uses this permeability inside the permanent magnet itself.

Since the HAM method uses a mesh-based MEC approach, the mesh density is an important factor in the HAM. As especially visible in Fig. 10(c), the meshing of the MEC region results in an discretization error. The discretization noise is caused by the fact that the coordinates, on which the magnetic flux density is extracted from the HAM, are not the points on which the magnetic scalar potential is calculated during solving. The mesh-based MEC modeling assumes an equal magnetic flux density inside each of the flux tubes shown in Fig. 6, therefore, the most accurate result is obtained in the potential node. Between two potential nodes, the magnetic flux density is assumed constant, which results in a staircase-shaped flux density. To reduce this discretization error, the number of MEC elements inside the MEC region could be increased.

Another deviation caused by the discretization is visible around the edges of the materials, clearly shown in Fig. 11(b). On the edges of the materials, the magnetic permeability will change rapidly. Due to the calculation of the magnetic flux

according to (24)–(27), the changing permeability will be visible between the two potential nodes located around the material edge. By decreasing the size of the MEC elements around the edges of the materials, the deviation of the magnetic flux density around these edges is decreased.

Only linear materials are assumed in the shown formulation, which results in the very large magnetic flux density occurring inside the magnetic shield of Fig. 9(a). These magnetic flux density values will most definitely cause saturation inside the magnetic shield. Saturation effects are not included in the modeling; however, based on an iterative process, the magnetic permeability of the materials inside the MEC layer can be changed. Therefore, local saturation effects can be included in the MEC region of the HAM, while only global saturation effects can be included in most other analytical modeling methods.

As previously indicated, the accuracy of the magnetic flux density results increases when the number of harmonics considered is increased. However, due to the large difference in values in the E -matrix (60), which are caused by the positive and negative exponential values in the Fourier modeling, singularity in the matrix might occur. This singularity limits the number of harmonics, since the harmonic number n is used in the exponential terms.

An increase in the number of MEC elements gives a more accurate solution, however, increasing the mesh density, in equality with FEA, will result in a larger computational effort. From a computational point of view, the proposed HAM is less computationally intensive with respect to FEA, especially since only a part of the domain is meshed. A large additional reduction of the computational efforts is possible in the HAM, since the current implementation is not optimized for calculation time. For both the FEA and the HAM, a tradeoff should be made between the desired mesh density and the resulting calculation times. However, since the HAM only meshes the regions with changing material properties, the air gap of a motor is not meshed, while especially in the air gap of a machine, a high mesh density in FEA is required for an accurate result.

A significant reduction in calculation time of the magnetic field and force is possible for certain variations. Since all source terms (i.e., the magnetization and current density terms) are collected in the Y_{tot} -matrix, the variations of the source amplitude and a movement of the source in the x -direction are included by only recalculating Y_{tot} . A movement of a source in the z -direction or movement of (and movement within) the MEC region requires recalculation of the full system of linear equations.

The proposed modeling method is not only suited for geometries in Cartesian coordinate systems. With the adaption of the harmonic description according to [9], polar and cylindrical coordinate systems are possible as well.

IX. CONCLUSION

The principle of combining Fourier modeling with mesh-based MEC modeling is demonstrated on two electromagnetic examples. It is shown that the HAM technique can be applied to any geometry where a periodicity

is present or can be assumed in Cartesian coordinate systems. With the inclusion of the mesh-based MEC modeling, the possibilities and applicability of the modeling for geometries with small features of high-permeable material, such as saliency, tooth shoes, and slot shapes, is increased. Since HAM describes the air-gap region of a machine by means of a Fourier series, it requires a less dense meshing compared with FEA.

For the electromagnetic example structures, shown in this paper, excellent agreement is obtained with respect to FEA, which proves the applicability of this modeling method for a wide class of electromagnetic devices. For the forces calculated with the hybrid analytical model, <3 [%] deviation with respect to FEA is obtained.

REFERENCES

- [1] J. L. Coulomb, "A methodology for the determination of global electromechanical quantities from a finite element analysis and its application to the evaluation of magnetic forces, torques and stiffness," *IEEE Trans. Magn.*, vol. 19, no. 6, pp. 2514–2519, Nov. 1983.
- [2] H. C. Roters, *Electromagnetic Devices*. New York, NY, USA: Wiley, 1941.
- [3] V. Ostović, *Dynamics of Saturated Electric Machines*. New York, NY, USA: Springer-Verlag, 1989.
- [4] E. P. Furlani, *Permanent Magnet and Electromechanical Devices*, I. Mayergoyz, Ed. Amsterdam, The Netherlands: Elsevier, 2001.
- [5] J. L. G. Janssen, B. L. J. Gysen, J. J. H. Paulides, and E. A. Lomonova, "Advanced electromagnetic modeling applied to anti-vibration systems for high precision and automotive applications," *Int. Compumag Soc. Newslett.*, vol. 19, no. 1, pp. 3–16, Jan. 2012.
- [6] G. Akoun and J.-P. Yonnet, "3D analytical calculation of the forces exerted between two cuboidal magnets," *IEEE Trans. Magn.*, vol. 20, no. 5, pp. 1962–1964, Sep. 1984.
- [7] M. F. J. Kremers, J. J. H. Paulides, E. Ilhan, J. L. G. Janssen, and E. A. Lomonova, "Relative permeability in a 3D analytical surface charge model of permanent magnets," *IEEE Trans. Magn.*, vol. 49, no. 5, pp. 2299–2302, May 2013.
- [8] B. Hague, "The principles of electromagnetism, applied to electrical machines," in *Electromagnetic Problems in Electrical Engineering*, 1st ed. New York, NY, USA: Dover, 1962.
- [9] B. L. J. Gysen, K. J. Meessen, J. J. H. Paulides, and E. A. Lomonova, "General formulation of the electromagnetic field distribution in machines and devices using Fourier analysis," *IEEE Trans. Magn.*, vol. 46, no. 1, pp. 39–52, Jan. 2010.
- [10] J. Caldwell, "Modifications of the Fourier approach for magnetic field calculations to include axial shields in superconducting magnets," *J. Appl. Phys.*, vol. 56, no. 11, pp. 3338–3340, 1984.
- [11] K. J. W. Pluk, J. W. Jansen, and E. A. Lomonova, "Magnetic shielding for coreless linear permanent magnet motors," *Appl. Mech. Mater.*, vols. 416–417, pp. 45–52, Sep. 2013.
- [12] M. F. J. Kremers, E. Ilhan, D. C. J. Krop, J. J. H. Paulides, and E. A. Lomonova, "Reluctance network model for the in-wheel motor of a series-hybrid truck using tooth contour method," in *Proc. 14th Biennial IEEE Conf. Electromagn. Field Comput. (CEFC)*, May 2010, p. 1.
- [13] E. Ilhan, M. F. J. Kremers, E. T. Motoasca, J. J. H. Paulides, and E. A. Lomonova, "Spatial discretization methods for air gap permeance calculations in double salient traction motors," *IEEE Trans. Ind. Appl.*, vol. 48, no. 6, pp. 2165–2172, Nov./Dec. 2012.
- [14] G. Xiong and S. A. Nasar, "Analysis of fields and forces in a permanent magnet linear synchronous machine based on the concept of magnetic charge," *IEEE Trans. Magn.*, vol. 25, no. 3, pp. 2713–2719, May 1989.
- [15] J. M. M. Rovers, J. W. Jansen, and E. A. Lomonova, "Modeling of relative permeability of permanent magnet material using magnetic surface charges," *IEEE Trans. Magn.*, vol. 49, no. 6, pp. 2913–2919, Jun. 2013.
- [16] D. T. E. H. van Casteren, J. J. H. Paulides, and E. A. Lomonova, "3-D numerical surface charge model including relative permeability: The general theory," *IEEE Trans. Magn.*, vol. 50, no. 11, Nov. 2014, Art. ID 8204704.
- [17] K. J. W. Pluk, G. De Gersem, J. W. Jansen, and E. A. Lomonova, "Fourier modeling of magnetic shields with linear permeable material and finite dimensions," *IEEE Trans. Magn.*, vol. 49, no. 7, pp. 4160–4163, Jul. 2013.
- [18] M. Amrhein and P. T. Krein, "3-D magnetic equivalent circuit framework for modeling electromechanical devices," *IEEE Trans. Energy Convers.*, vol. 24, no. 2, pp. 397–405, Jun. 2009.
- [19] C. B. Rasmussen and E. Ritchie, "A magnetic equivalent circuit approach for predicting PM motor performance," in *Proc. Conf. Rec. IEEE 32nd IAS Annu. Meeting, Ind. Appl. Conf. (IAS)*, vol. 1, Oct. 1997, pp. 10–17.
- [20] J. Perho, *Reluctance Network for Analysing Induction Machines* (Electrical Engineering). Espoo, Finland: Finnish Academies of Technology, 2002.
- [21] S. Ouagued, Y. Amara, and G. Barakat, "Comparison of hybrid analytical modelling and reluctance network modelling for pre-design purposes," in *Proc. ELECTRIMACS*, 2014, pp. 238–243.
- [22] G. Barakat and Y. Amara, "A simple and effective way to couple analytical formal solution of magnetic potential and reluctance network models," in *Proc. 9th IET Int. Conf. Comput. Electromagn. (CEM)*, Mar. 2014, pp. 1–2.
- [23] Y. Laoubi, M. Dhifli, G. Verez, Y. Amara, and G. Barakat, "Open circuit performance analysis of a permanent magnet linear machine using a new hybrid analytical model," *IEEE Trans. Magn.*, vol. 51, no. 3, pp. 1–4, Mar. 2015.
- [24] M. Mirzayee, H. Mehrjerdi, and I. Tsurkerman, "Analysis of a high-speed solid rotor induction motor using coupled analytical method and reluctance networks," in *Proc. IEEE/ACES Int. Conf. Wireless Commun. Appl. Comput. Electromagn.*, Apr. 2005, pp. 537–540.
- [25] J. Cai, Q. Lu, Y. Jin, C. Chen, and Y. Ye, "Performance investigation of multi-tooth flux-switching PM linear motor," in *Proc. Int. Conf. Elect. Mach. Syst. (ICEMS)*, Aug. 2011, pp. 1–6.
- [26] K. J. W. Pluk, J. W. Jansen, and E. A. Lomonova, "Force measurements on a shielded coreless linear permanent magnet motor," *IEEE Trans. Magn.*, vol. 50, no. 11, pp. 1–4, Nov. 2014, Art. ID 8500404.
- [27] *FLUX 12.0, User's guide*, Cedrat, Meylan, France, 2015.
- [28] J. W. Gibbs, "Fourier series," *Nature*, vol. 59, p. 200, 1898.